Proceedings of the ASME 2018 37th International Conference on Ocean, Offshore and Arctic Engineering
OMAE2018
June 17-22, 2018, Madrid, Spain

OMAE2018-78070

FLUID PARAMETER IDENTIFICATION FOR UNDERWATER SNAKE ROBOTS

Eleni Kelasidi *†
Department of Engineering Cybernetics,
Norwegian University of Science and Technology,
NO-7491 Trondheim, Norway
Email: eleni.kelasidi@ntnu.no

Gard Elgenes
Henrik Kilvær

Department of Engineering Cybernetics,
Norwegian University of Science and Technology,
NO-7491 Trondheim, Norway

ABSTRACT

Nowadays different types of unmanned underwater vehicles (UUVs), such as remotely operated vehicles (ROVs) and autonomous underwater vehicles (AUVs), are widely used for subsea inspection, maintenance, and repair (IMR) operations in the oil and gas industry, archaeology, oceanography and marine biology. Also, lately, the development of underwater snake robots (USRs) shows promising results towards extending the capabilities of conventional UUVs. The slender and multi-articulated body of USRs allows for operation in tight spaces where other traditional UUVs are incapable of operating. However, the mathematical model of USRs is more challenging compared to models of ROVs and AUVs, because of its multi-articulated body. It is important to develop accurate models for control design and analysis, to ensure the desired behaviour and to precisely investigate the locomotion efficiency. Modelling the hydrodynamics poses the major challenge since it includes complex and nonlinear hydrodynamic effects. The existing analytical models for USRs consider theoretical values for the fluid coefficients and thus they only provide a rough prediction of the effects of hydrodynamics on swimming robots. In order to obtain an accurate prediction of the hydrodynamic forces acting on the links of the USRs, it is necessary to obtain the fluid coefficients experimentally. This paper determines the drag and added mass coefficients of a general planar model of USRs. In particular, this paper presents methods for identifying fluid parameters based on both computational fluid dynamic (CFD) simulations and several experimental approaches. Additionally, in this paper, we investigate variations of the drag force modelling, providing more accurate representations of the hydrodynamic drag forces. The obtained fluid coefficients are compared to the existing estimates of fluid coefficients for a general model of USRs.

INTRODUCTION

The last decades, remotely operated vehicles (ROVs) and autonomous underwater vehicles (AUVs) are widely used for different subsea operations, as they can operate at larger depths and at more hazardous environments than humans [1]. In addition, development of bio-inspired USRs are of interest, as they are more agile and can be more energy efficient than traditional ROVs and AUVs. Bio-inspired snake robots having flexible and slender bodies can further operate at tighter and more obstructed areas than other underwater vehicles. In addition to the agility and small cross-section of USRs, they are essentially mobile manipulator arms capable of doing a large variety of tasks. In addition, the snakes can be docked at underwater charging stations, resulting in a shorter response time when they are needed to perform a task. These properties make them well-suited for a large variety of tasks [2].

Bio-inspired snake robots have been studied for many years and the first snake robot was made by Hirose in 1972 [3]. Several models for land-based snake robots has been proposed in the literature [4]. The hydrodynamic modeling of USRs is more

*This work was funded by the Research Council of Norway through its Centres of Excellence funding scheme, project no. 223254-NTNU AMOS, and by VISTA - a basic research program in collaboration between The Norwegian Academy of Science and Letters, and Statoil.

†Address all correspondence to this author.

complex than for other underwater vehicles due to their multi-articulated body. In particular, modeling of the fluid contact forces are especially more complicated compared to the dynamics of the overall rigid motion, making them more complex than land-based snake robots. Due to hydrodynamic complexity, there have been proposed fewer models for USRs than the land-based snake robots [2]. Hence, the main objective of this paper is to provide useful inputs regarding the hydrodynamic model of USRs by experimentally obtaining the fluid coefficients.

A key issue in development and control of USRs, is to achieve high motion-effectiveness and speed, while minimizing the consumed energy. The optimization of gait patterns is still to a large degree an unanswered question in the literature, although some results have been proposed [5, 6]. The existing results [5], provide only qualitative comparisons of the gait pattern efficiency, as theoretical values for the fluid coefficients are being used. Since fluid friction plays a significant role on the power consumption, a correct fluid model is desired. By identifying the fluid friction parameters, the energy efficiency of USRs can be investigated and provide qualitative as well as quantitative comparison results regarding the power consumption. As the locomotion efficiency of an USR is closely coupled with the hydrodynamic effects, there is a need for obtaining the fluid coefficients included in the model. Fluid torques have a direct impact on the power consumption of the system, and including these will improve the model from a hydrodynamic and energy efficiency point of view [7], [2]. Experimental validation of a complex model that takes into account both added-mass effects and drag forces while being expressed in closed-form has not yet been investigated in the literature [2]. The existing models for USRs use theoretical values of the fluid coefficients [2, 8]. The authors in [2] pointed out the need for further investigation into the method for fluid coefficient identification to obtain more precise values of the drag and added mass coefficients. It is therefore necessary to obtain and calculate the fluid coefficients experimentally in order to obtain fairly accurate models of the fluid effects when modeling multi-articulated biologically inspired USRs.

This paper compares existing experimental methods and determines fluid coefficients for the underwater snake robot Mamba [2] in order to obtain an accurate hydrodynamic model for underwater swimming snake robots. The fluid coefficients are determined initially based on extensive computational fluid dynamics (CFD) simulations, and then compared to experimentally obtained results. Additionally, in this paper we investigate variations of the drag force models, providing more accurate representations of the hydrodynamic drag forces. The obtained fluid coefficients are compared to the existing estimates of fluid coefficients for a general model of USRs. In [8], only the drag forces from linear and nonlinear drag effects are considered in the hydrodynamic model. However, in this paper the hydrodynamic model is extended by variations including different combinations of linear and quadratic drag, contributions in x forces from flow in $y-$ direction, and effects caused by the head and tail modules.

HYDRODYNAMIC MODEL

This section gives a brief insight to the hydrodynamic model proposed for USRs in [8]. Compared to the model in [8] several variations are explored in this paper that include the head and tail in addition to the link modules. The model is further extended to include individual drag coefficients for linear and quadratic drag. In addition, a coupling between the velocity in body $y-$direction and the force in body $x-$direction is introduced. In [8] it is shown that the fluid forces on all links can be expressed in vector form as

$$\mathbf{f} = \begin{bmatrix} \mathbf{f_x} \\ \mathbf{f_y} \end{bmatrix} = \begin{bmatrix} \mathbf{f_{A_x}} \\ \mathbf{f_{A_y}} \end{bmatrix} + \begin{bmatrix} \mathbf{f^{I}_{D_x}} \\ \mathbf{f^{I}_{D_y}} \end{bmatrix} + \begin{bmatrix} \mathbf{f^{II}_{D_x}} \\ \mathbf{f^{II}_{D_y}} \end{bmatrix}, \tag{1}$$

where $\mathbf{f^{I}_{D_x}}$, $\mathbf{f^{I}_{D_y}}$, $\mathbf{f^{II}_{D_x}}$, $\mathbf{f^{II}_{D_y}}$ and $\mathbf{f_{A_x}}$, $\mathbf{f_{A_y}}$ represent the effects from the linear, the nonlinear drag forces and the added mass effects respectively, and are given by

$$\begin{bmatrix} \mathbf{f^{I}_{D_x}} \\ \mathbf{f^{I}_{D_y}} \end{bmatrix} = -\begin{bmatrix} \mathbf{c}_T\mathbf{C}_\theta & -\mathbf{c}_N\mathbf{S}_\theta \\ \mathbf{c}_T\mathbf{S}_\theta & \mathbf{c}_N\mathbf{C}_\theta \end{bmatrix} \begin{bmatrix} \mathbf{V_{r_x}} \\ \mathbf{V_{r_y}} \end{bmatrix}, \tag{2}$$

$$\begin{bmatrix} \mathbf{f^{II}_{D_x}} \\ \mathbf{f^{II}_{D_y}} \end{bmatrix} = -\begin{bmatrix} \mathbf{c}_T\mathbf{C}_\theta & -\mathbf{c}_N\mathbf{S}_\theta \\ \mathbf{c}_T\mathbf{S}_\theta & \mathbf{c}_N\mathbf{C}_\theta \end{bmatrix} \mathrm{sgn}\left(\begin{bmatrix} \mathbf{V_{r_x}} \\ \mathbf{V_{r_y}} \end{bmatrix} \right) \begin{bmatrix} \mathbf{V_{r_x}}^2 \\ \mathbf{V_{r_y}}^2 \end{bmatrix}, \tag{3}$$

$$\begin{bmatrix} \mathbf{f_{A_x}} \\ \mathbf{f_{A_y}} \end{bmatrix} = -\begin{bmatrix} \mathbf{C}_\theta & -\mathbf{S}_\theta \\ \mathbf{S}_\theta & \mathbf{C}_\theta \end{bmatrix} \begin{bmatrix} \mathbf{0} & \mathbf{0} \\ \mathbf{0} & \mu \end{bmatrix} \begin{bmatrix} \dot{\mathbf{V}}_{\mathbf{r_x}} \\ \dot{\mathbf{V}}_{\mathbf{r_y}} \end{bmatrix}, \tag{4}$$

where the relative velocities and accelerations in the body frame are given by

$$\begin{bmatrix} \mathbf{V_{r_x}} \\ \mathbf{V_{r_y}} \end{bmatrix} = \begin{bmatrix} \mathbf{C}_\theta & \mathbf{S}_\theta \\ -\mathbf{S}_\theta & \mathbf{C}_\theta \end{bmatrix} \begin{bmatrix} \dot{\mathbf{X}} - \mathbf{V}_x \\ \dot{\mathbf{Y}} - \mathbf{V}_y \end{bmatrix}, \tag{5}$$

$$\begin{bmatrix} \dot{\mathbf{V}}_{\mathbf{r_x}} \\ \dot{\mathbf{V}}_{\mathbf{r_y}} \end{bmatrix} = \begin{bmatrix} \mathbf{C}_\theta & \mathbf{S}_\theta \\ -\mathbf{S}_\theta & \mathbf{C}_\theta \end{bmatrix} \begin{bmatrix} \ddot{\mathbf{X}} \\ \ddot{\mathbf{Y}} \end{bmatrix} + \begin{bmatrix} -\mathbf{S}_\theta & \mathbf{C}_\theta \\ -\mathbf{C}_\theta & -\mathbf{S}_\theta \end{bmatrix} \begin{bmatrix} \mathrm{diag}(\dot{\theta}) & \mathbf{0} \\ \mathbf{0} & \mathrm{diag}(\dot{\theta}) \end{bmatrix} \begin{bmatrix} \dot{\mathbf{X}} - \mathbf{V}_x \\ \dot{\mathbf{Y}} - \mathbf{V}_y \end{bmatrix}, \tag{6}$$

where $\mathbf{V}_x = \mathbf{e}V_x \in \mathbb{R}^n$ and $\mathbf{V}_y = \mathbf{e}V_y \in \mathbb{R}^n$ with V_x and V_y representing the ocean current velocities in the inertial $x-$ and $y-$direction, respectively, and $\mathbf{e} = [1,\ldots,1]^T$. The vector $\theta = [\theta_1,\ldots,\theta_n]$ represent the link angles of the robot with n representing the links numbers of the robot. The matrices $\mathbf{c}_T = \mathrm{diag}\,(c_{T,1},\ldots,c_{T,n}) \in \mathbb{R}^{n\times n}$ and $\mathbf{c}_N = \mathrm{diag}\,(c_{N,1},\ldots,c_{N,n}) \in \mathbb{R}^{n\times n}$ represent the drag parameters in the tangent and normal direction of each link, and $\mu = \mathrm{diag}\,(\mu_1,\ldots,\mu_n) \in \mathbb{R}^{n\times n}$ represents the added mass parameters.

Furthermore, the fluid torques on all links are given by

$$\tau = -\Lambda_1\ddot{\theta} - \Lambda_2\dot{\theta} - \Lambda_3\dot{\theta}|\dot{\theta}|, \tag{7}$$

where $\Lambda_1 = \mathrm{diag}\,(\lambda_{1,1},\ldots,\lambda_{1,n}) \in \mathbb{R}^{n\times n}$, $\Lambda_2 = \mathrm{diag}\,(\lambda_{2,1},\ldots,\lambda_{2,n}) \in \mathbb{R}^{n\times n}$ and $\Lambda_3 = \mathrm{diag}\,(\lambda_{3,1},\ldots,\lambda_{3,n}) \in \mathbb{R}^{n\times n}$. The coefficients $\lambda_{2,i}$, $\lambda_{3,i}$ represent the drag torque parameters, and the parameter $\lambda_{1,i}$ represents the added mass parameter.

In [8] it is shown that the hydrodynamic related parameters for the cylindrical links with major diameter $2e_{1i}$, the minor diameter $2e_{2i}$ and the length of each link $2l_i$, can be expressed as:

$$\begin{aligned} c_{T,i} &= \frac{1}{2}\rho\pi C_f \frac{(e_{2i}+e_{1i})}{2} 2l_i, \quad c_{N,i} = \frac{1}{2}\rho C_D 2e_{1i} 2l_i, \\ \mu_i &= \rho\pi C_A e_{1i}^2 2l_i, \quad \lambda_{1,i} = \frac{1}{12}\rho\pi C_M (e_{1i}^2 - e_{2i}^2)^2 l_i^3, \\ \lambda_{2,i} &= \frac{1}{6}\rho\pi C_f (e_{1i}+e_{2i}) l_i^3, \quad \lambda_{3,i} = \frac{1}{8}\rho\pi C_f (e_{1i}+e_{2i}) l_i^4, \end{aligned} \tag{8}$$

for $i \in 1,\ldots,n$ where C_f and C_D are the drag coefficients, while C_A and C_M represent the added mass related coefficients, and ρ is the density of the fluid. For more details see [8]. Note that the fluid parameters are dependent on the fluid coefficients C_f, C_D, C_A, which this paper aims to identify.

Remark 1. *Based on extensive comparison between experimental results and model simulations in [2] the following estimates have been used so far for the underwater snake robot Mamba: a) estimated values: $C_f = 0.3$, $C_D = 1.75$, $C_A = 1.5$ and $C_M = 1$ and b) theoretical values: $C_f = 0.01 - 0.03$, $C_D = 1$, $C_A = 1$ and $C_M = 1$. These values are chosen under the assumption of a steady-state flow [9], [7], which results in setting the added mass inertia coefficient to its theoretical value, $C_M = 1$, as the overall motion of the system is not significantly affected by this coefficient. Hence in this paper we have not considered identifying the added mass inertia coefficient C_M.*

The hydrodynamic model given by (1) considers USRs with n links. This model can be expanded in different forms. By using (2) and (3) and the simplified velocity notations v_x and v_y in the $x-$ and $y-$ direction, the total drag force for an USR with n links can be written as

$$\mathbf{f}_1 = -n \begin{bmatrix} \frac{1}{2}\pi\rho(\frac{(a_i+b_i)}{2})2l_iC_f & 0 \\ 0 & \frac{1}{2}\rho 2a_i 2l_i C_d \end{bmatrix} \left(\begin{bmatrix} v_x \\ v_y \end{bmatrix} + \begin{bmatrix} \text{sgn}(v_x)v_x^2 \\ \text{sgn}(v_y)v_y^2 \end{bmatrix} \right), \quad (9)$$

where $\mathbf{f}_1$ is the original drag force model proposed in [8] considering the same geometrical characteristics for the modules of the robot. The first variation, $\mathbf{f}_2$, distinguishes between the drag coefficients for linear and quadratic drag, while still assuming that the modules of the USR has same geometries and can be expressed as follows

$$\begin{aligned} \mathbf{f}_2 = -n\mathbf{f}_D = n\left(\mathbf{f}^{\text{I}}_{D,L} + \mathbf{f}^{\text{II}}_{D,L}\right) = -n \begin{bmatrix} \frac{1}{2}\pi\rho(\frac{(a_i+b_i)}{2})2l_iC^{\text{I}}_f & 0 \\ 0 & \frac{1}{2}\rho 2a_i 2l_i C^{\text{I}}_d \end{bmatrix} \begin{bmatrix} v_x \\ v_y \end{bmatrix} \\ -n \begin{bmatrix} \frac{1}{2}\pi\rho(\frac{(a_i+b_i)}{2})2l_iC^{\text{II}}_f & 0 \\ 0 & \frac{1}{2}\rho 2a_i 2l_i C^{\text{II}}_d \end{bmatrix} \begin{bmatrix} \text{sgn}(v_x)v_x^2 \\ \text{sgn}(v_y)v_y^2 \end{bmatrix}. \end{aligned} \quad (10)$$

The next model variation also includes the linear and quadratic drag terms for the head and tail modules, and is given by

$$\begin{aligned} \mathbf{f}_3 = -(n-2)\mathbf{f}_D - \begin{bmatrix} \frac{1}{2}\pi\rho a_i b_i C^{\text{I}}_{f_{HT}} & 0 \\ 0 & \frac{1}{2}\rho A_{HT} C^{\text{I}}_{d_{HT}} \end{bmatrix} \begin{bmatrix} v_x \\ v_y \end{bmatrix} \\ - \begin{bmatrix} \frac{1}{2}\pi\rho a_i^2 C^{\text{II}}_{f_{HT}} & 0 \\ 0 & \frac{1}{2}\rho A_{HT} C^{\text{II}}_{d_{HT}} \end{bmatrix} \begin{bmatrix} \text{sgn}(v_x)v_x^2 \\ \text{sgn}(v_y)v_y^2 \end{bmatrix} \end{aligned} \quad (11)$$

where A_{HT} is the characteristic area of the head and tail modules in y direction, and $C^{\text{I}}_{f_{HT}}$, $C^{\text{II}}_{f_{HT}}$, $C^{\text{I}}_{d_{HT}}$, $C^{\text{II}}_{d_{HT}}$ are the linear and nonlinear drag coefficients for the combined head and tail modules.

The following model variation additionally includes effects on forces in $x-$direction from v_y velocities:

$$\mathbf{f}_4 = \mathbf{f}_3 + \mathbf{f}^{\text{I}}_{D,XY} + \mathbf{f}^{\text{II}}_{D,XY} = \mathbf{f}_3 - \begin{bmatrix} 0 & -\text{sgn}(v_y)\rho a_i l_i C^{\text{I}}_{XY} \\ 0 & 0 \end{bmatrix} \begin{bmatrix} v_x \\ v_y \end{bmatrix} - \begin{bmatrix} 0 & \rho a_i l_i C^{\text{II}}_{XY} \\ 0 & 0 \end{bmatrix} \begin{bmatrix} v_x^2 \\ v_y^2 \end{bmatrix} \quad (12)$$

where C^{I}_{XY}, C^{II}_{XY} are the linear and nonlinear drag coefficients.

The next variation omits the linear drag effects for the head and tail modules as well as for the cross terms:

$$\mathbf{f}_5 = \mathbf{f}^{\text{II}}_{D,HT} + (n-2)\mathbf{f}_D + \mathbf{f}^{\text{II}}_{D,XY}. \quad (13)$$

The last model variation is built on the general fluid drag force model by considering only the nonlinear drag effects:

$$\mathbf{f}_6 = \begin{bmatrix} \frac{1}{2}\rho A_x C_f v_x^2 & 0 \\ 0 & \frac{1}{2}\rho A_y(n) C_d v_y^2 \end{bmatrix}, \quad (14)$$

where $A_x = \pi a_i b_i$ and $A_y = A_{y,H} + n2l_i2a_i + A_{y,T}$ are the reference areas in $x-$ and $y-$direction, and where $A_{y,H}$ and $A_{y,T}$ are the reference areas for the head and tail modules of the robot.

The different model variations of the drag model will be investigated in this paper based on the obtained forces from the simulations and experiments. In particular, this paper identifies the fluid parameters for the different model variations by considering the numerous possible drag coefficients shown in Table 1 for the model variations presented in (9)-(14). To estimate the drag coefficients for the models given by (9)-(14), a least-square estimation scheme is used [10, 11]. For more details see [11].

Model	Corresponding fluid coefficients
$\mathbf{f}_1$	C_f, C_d
$\mathbf{f}_2$	$C^{\text{I}}_f, C^{\text{I}}_d, C^{\text{II}}_f, C^{\text{II}}_d$
$\mathbf{f}_3$	$C^{\text{I}}_f, C^{\text{I}}_d, C^{\text{II}}_f, C^{\text{II}}_d, C^{\text{I}}_{f_{HL}}, C^{\text{I}}_{d_{HL}}, C^{\text{II}}_{f_{HL}}, C^{\text{II}}_{d_{HL}}$
$\mathbf{f}_4$	$C^{\text{I}}_f, C^{\text{I}}_d, C^{\text{II}}_f, C^{\text{II}}_d, C^{\text{I}}_{f_{HL}}, C^{\text{I}}_{d_{HL}}, C^{\text{II}}_{f_{HL}}, C^{\text{II}}_{d_{HL}}, C^{\text{I}}_{XY}, C^{\text{II}}_{XY}$
$\mathbf{f}_5$	$C^{\text{I}}_f, C^{\text{I}}_d, C^{\text{II}}_f, C^{\text{II}}_d, C^{\text{II}}_{f_{HL}}, C^{\text{II}}_{d_{HL}}, C^{\text{II}}_{XY}$
$\mathbf{f}_6$	C_f, C_d

TABLE 1: Fluid coefficients for model variations.

FLUID PARAMETER IDENTIFICATION METHODS

There are several approaches for identifying fluid coefficients for submerged bodies, both by theoretical estimates and experimental procedures. This section presents some of the possible methods for fluid parameter identification and concludes with, the adopted methods in this paper. Results can be obtained for the fluid drag coefficients based either on computational fluid dynamics (CFD) simulations or experiments. Multiple software solutions are available, such as ANSYS Fluent, OpenFOAM and the flow simulation package in Solidworks [11]. Solidworks is chosen in this paper as it is fairly straight forward to simulate on existing computer-aided design (CAD) models of the USR Mamba [2] and since the flow simulation package is quite powerful, and high mesh settings may provide very accurate results [11]. For obtaining the added mass coefficients, the following two software candidates can be used: Wave Analysis by Massachusetts Institute of Technology (WAMIT) and wave analysis by diffraction and morison theory (WADAM). Other approaches for identifying the added mass coefficients such as strip theory and empirical 3D data can be used. Strip theory evaluates a 3D object as a sum of 2D strips and assumes a slender body where the length is much larger than the width [11]. However, this will

not be the case for a snake robot with few links. WADAM and WAMIT are widely used to obtain the added mass coefficients in marine vehicles or floating structures [12], [13]. Note that WAMIT lacks a graphical user interface, and thus WADAM is considered in this paper as the 3D potential theory in WADAM is directly based on WAMIT and has a good graphical user interface.

Different methods for experimentally determining the fluid coefficients can be found in the literature. Below, some of the methods are overviewed:

Free decay pendulum motion: The free decay pendulum test uses a scaled-down model of the vehicle as a pendulum connected by a rod [14]. It is set to oscillate in water when it is displaced from its equilibrium position. Due to the hydrodynamic forces that resist the motion, the amplitude of the swinging motion will decay over time. The hydrodynamic parameters can then be extracted from the history of the motion. In this approach, there is a need of accurately measuring the position and the states of the vehicle, which can be challenging.

Towing test and rotation test: This approach is often used for ship design [15]. An object is towed at different velocities to determine quadratic and linear damping terms. In addition, accelerated runs are performed for different accelerations. By measuring forces at different velocities and subtracting the already known damping and rigid body mass forces, added mass forces can be obtained. The procedure can be repeated for rotational experiment. This approach is quite easy to perform. However, it is quite time consuming.

Guided rail: A guided rail experiment acts on the same principle as the towing test, but by instead uses a guided rail in an enclosed tank. The module is connected to the rail and moves in the tank. By measuring the forces applied, it is possible to extract the hydrodynamic parameters [16].

On-board sensor experiments: In this approach the accelerations of the system can be measured for a given thrust input. Inertia and damping terms can then be obtained by filtering the acceleration data [17].

Planar motion mechanism tests: A planar motion mechanism is an electromechanical device used to move a model ship in a pre-programmed series of motions in a test tank facility. The forces and moments on the model, and other data related to the performance of the model can be measured and used to identify the fluid parameters [18].

Based on available resources and equipment, in this paper three performed experiments are described. For identification of the drag coefficients, two variations of the above concepts are considered: a) a simplified guided rail approach and b) experiments based on the towing test and guided rail approaches. The experimental approach concerning added mass coefficients is inspired by the decaying pendulum, where the pendulum oscillations are actuated by a servo motor.

SIMULATION STUDIES

This section covers the theoretical identification of the fluid coefficients based on the simulations conducted in Solidworks and WADAM. The geometry of the USR Mamba [2] has been considered in the simulations with module configurations ranging from the head and tail modules with one link (H1LT) up to nine links (H9LT). Note that by varying the number of links, it is possible to investigate how the identified fluid coefficients are dependent on the length of the robot. The theoretical values for the drag coefficients are calculated using the flow simulation extension of Solidworks. Generally, for the CFD simulations it is hard to find the optimal mesh since this should be chosen considering a trade-off between accuracy and simulation time. In this paper, the simulations were performed with mesh setting 6. This secures relatively accurate results, but demands long computing time [11]. Regarding the computational domain (CD), several tests were done analysing the pressure and velocity profiles around the geometry to determine the smallest possible CD without the loss of information. Detailed discussion for the proper choice of mesh and CD can be found in [11]. Simulations have been performed for several cases with different snake module configurations. Table 2 gives an overview of the simulation cases performed on each body configuration H1LT through H9LT.

	Velocity [m/s]		**Angle** θ [deg]		No. of
	Range	Step size	Range	Step size	simulations
Case 1	[0.02 to 1]	0.02	0	—	50
Case 2	0.1	—	[0 to 90]	3	31
Case 3	0.2	—	[0 to 90]	3	31
Case 4	0.3	—	[0 to 90]	3	31
Case 5	0.4	—	[0 to 90]	3	31
Simulation scenarios per configuration: 174					
Total number of simulations: 1566					

TABLE 2: Simulation cases for drag coefficients for each body configuration H1LT through H9LT.

As already mentioned, for the added mass coefficients identification the software extension WADAM is adopted in this paper. The frequency-independent added mass matrix is of interest, hence using a water depth of 300 meters, the snake is placed 100 meters below the water surface. It can thus be assumed that the added mass coefficients are not influenced by the wave frequency and are constant, making the added mass purely dependent on the acceleration of the body. A uniform mass distribution is assumed, and that the center of buoyancy (CB) is located at the center of mass (CM) of the body. For each simulation of the different snake configurations from H1LT to H9LT, the 6×6 dimensionless added mass matrix $\mathbf{A}^D$ is obtained. The non-dimensionless elements are found by multiplying with the water density and the

volume of the object:

$$\mathbf{A}_i^{ND} = \mathbf{A}_i^D \rho V_i, \tag{15}$$

where the superscript denotes non-dimensionless (ND) and dimensionless (D), V_i is the volume of body i, and the subscript $i \in \{H, T, HLT, H2LT, H3LT, ..., H9LT\}$ denotes the module or the configuration of modules. The first two diagonal elements of $\mathbf{A}^{ND}$ represent the added mass coefficient in $x-$direction, μ_t and in $y-$direction, μ_n, respectively.

EXPERIMENTAL SETUP

This section presents the experimental setups used for identification of the fluid coefficients, including the choice of a suitable force/torque sensor. The two chosen experiments incorporates a passive guided rail towing tank and a circulation tank. Note that for large objects, experiments are often conducted with scaled down models. As the snake module configurations are small, experiments are conducted for full-scale snake module configurations, and thus, the scaling errors are avoided.

An important aspect of the experimental approach for identifying the fluid coefficients is the ability to choose a suitable force/torque sensor. In addition, the physical placement of the sensor is a major factor to consider when selecting the sensor. The ideal case is to mount the sensor in direct proximity to the CM of the snake modules as this point is the center of all calculations, and thus the need for transforming the measurements will be eliminated. This concept was used in this paper in the experiments. Therefore, the waterproof sensor Mini40 with IP68 rating from ATI Industrial Automation is chosen for the experiments in this paper, which has a low-profile design ideal for several mounting scenarios. In addition, the sensor has a very low noise distortion due to the use of silicon strain gauges that provides a stronger signal than conventional strain gauges. For the experiments conduced in this paper, the sensor was connected to the experimental rig by a stiff rod. A connector plate was mounted between the rod and the sensor to securely fasten the sensor. Note that it is desirable to make the surface of the 3D printed modules as smooth as possible to match the simulation parameters. Hence, silicon coating is applied to achieve the smoothness of the module.

Passive guided rail gowing tank

The passive guided rail towing rig approach utilizes a relatively small pool and a towing rig driven by simple weights. As the system has a passive input in the form of an applied weight, there is no need for developing electromechanical control systems. This does however produce a challenge in estimating velocities as there is no direct control or measurement of it. The validity of the experiments depends on the system reaching a steady-state velocity when measuring the forces acting on the snake. However, this setup is adapted to perform preliminary experiments as it is relatively simple and sufficient to obtain initial results for the drag coefficients. Figure 1 gives an overview of this experimental setup.

Given a submerged body moving through water, if the force acting on the body can be measured, the following equation provides sufficient information to identify the fluid coefficients:

$$f_m = f_D + f_A + ma, \tag{16}$$

where f_m represents the measured forces, f_D the drag forces, f_A the added mass forces, m is the mass of the submerged body, and a represent the acceleration of the body. Assuming a constant velocity at steady state, the acceleration and added mass terms are zero and the above equation results in a direct measurement of the total drag forces. The drag term contains both linear and nonlinear (quadratic) drag forces. Further, if the velocity and angle of attack of the submerged body can be controlled, and in addition, the force acting on the body can be measured in body $x-$ and $y-$directions, then drag coefficients can be determined.

The experimental rig is built around a plastic pool of dimensions 1.5 m $\times$ 0.9 m $\times$ 1 m. The snake configuration is placed in the middle of the pool. The wagon and snake configuration is constricted to movement along the global $x-$axis, while the angle of attack can be adjusted by a mechanism on the wagon. A weight pulling a string fastened to the wagon is the actuator input to the system. The weight is suspended from the roof and is extended to the wagon via a string through two pulleys, allowing the weight to pull vertically while the motion of the wagon is horizontal. Two types of scenarios are run for each snake configuration. In the first scenario, the snake is traveling through the water tank with an angle of attack equal to zero, $\theta = 0$ degrees. This is done for a set of different weights as inputs. In the second scenario, the angle of attack is increased by 3 degrees for each run. This is done for three different weights, totaling in 39 data points.

As already mentioned, a precise velocity estimation is vital for producing correct results. The Canon Legria HFG30 video camera mounted on a tripod overlooking the end of the rail as seen in Figure 1 is used for velocity estimation in this paper. For more details see [11]. All experimental runs for the H1LT configuration at zero degree angle of attack are conducted six times, resulting in six individual runs for each weight configuration. This is done to validate the force measurements and velocity estimations, and investigate the repeatability of the experimental trials.

Circulation tank

In this approach, the snake robot configurations are submerged in a circulation tank. Similar to the passive towing tank experiment, force measurements are recorded. However, now the fluid velocity is constant and known. Furthermore, by moving the submerged snake configuration in a sinusoidal motion the added mass coefficient in $y-$direction can be identified. Given that the drag coefficients are identified, (16) can be exploited to extract the added mass coefficients. The method requires the acceleration of the snake configuration to be known. An assumption made for the mathematical model in [8] is that the robot

is neutrally buoyant. This is not the case for the conducted experiments. While this is of no importance for the drag related experiments, this can have a huge impact on the added mass experiments. Assuming the fully submerged snake module configuration has positive buoyancy, the following equation can be used to extract the added mass forces of the robot:

$$f_m = ma + f_D + f_A + f_B, \tag{17}$$

where f_B is the buoyancy force.

Figure 2 gives an overview of the circulation tank experiments. The snake module configuration is mounted submerged in a test section of a circulation tank. For the fluid drag coefficients identification, the angle of attack of the snake configuration can be chosen between 0 and 90 degrees. For added mass identification, the angle of attack is set at $\theta = 0$ degrees, while a servo motor moves the snake in a sinusoidal motion, like a pendulum, perpendicular to the flow. The body velocity and acceleration are extracted from the given input and measured servo motor angle. The velocity of the fluid is measured using a laser doppler velocimetry (LDV) setup [11].

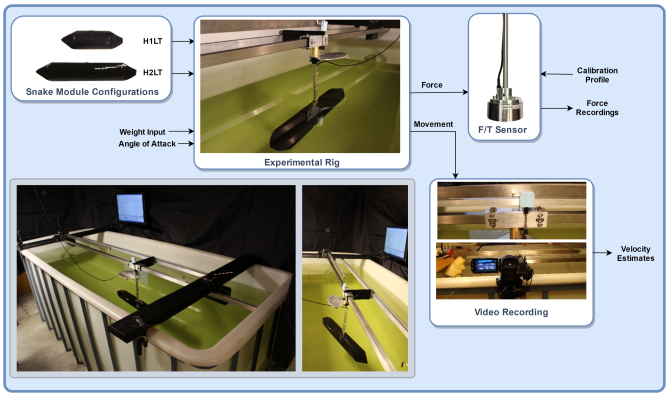

FIGURE 1: Overview of the passive guided rail towing tank experimental approach.

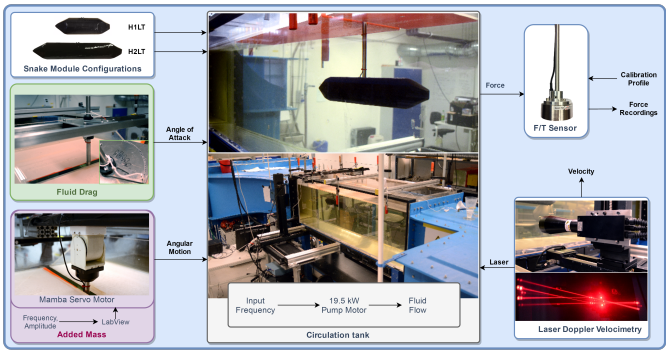

FIGURE 2: Overview of the circulation tank experimental approaches.

For the added mass experiments, the modules require an acceleration. This is achieved by utilizing a servo motor from the snake robot Mamba [2]. In particular, an actual functioning joint module from Mamba containing the servo motor, electronics and an angular positioning sensor is used for this purpose. The angular motion is achieved by using the following reference angle for the joint:

$$\phi_{ref} = \alpha \sin(\omega t), \tag{18}$$

where ω is the frequency and α is the amplitude.

The lag between the measured position ϕ and the command signal ϕ_{ref} is used to determine the phase shift, Φ. Note that the measured amplitude is larger than the commanded due to overshooting. The difference is adjusted for by adding a term to the amplitude. The corrected signal, ϕ_{ref}, can be differentiated to find the angular velocity and acceleration coinciding with the measured angle. The velocity and the acceleration in $y-$direction are found by multiplying with the radius, $r = 0.476$ m. The resulting velocity and acceleration estimates of the snake module configuration is given by

$$\begin{aligned} \hat{v}_y &= r(\alpha+\delta)\,\omega \sin(\omega t + \Phi), \\ \hat{a}_y &= -r(\alpha+\delta)\,\omega^2 \cos(\omega t + \Phi), \end{aligned} \tag{19}$$

where δ and Φ are the amplitude and phase shift correction terms, respectively.

	Velocity [m/s]		**Angle,** θ [deg]		No. of
	Range	step size	Range	Step size	runs
Case 1	[0.1 to 1]	0.1	0	—	10×2
Case 2	0.1	—	[0 to 90]	3	31×2
Case 3	0.2	—	[0 to 90]	3	31×2
Case 4	0.3	—	[0 to 90]	3	31×2
Case 5	0.4	—	[0 to 90]	3	31×2
Simulation scenarios per configuration: 134×2					
Total number of experimental runs: 536					

TABLE 3: Scenarios for obtaining drag coefficients in the circulation tank experiments for configurations H1LT and H2LT.

The experimental scenarios in circulation tank for identification of drag coefficients are chosen to match the simulation scenarios. The accurate control and measurement of the fluid flow velocity makes this possible. Table 3 shows the conducted experiments. Each of the experimental cases is conducted twice. Added mass experiments are conducted for a set of different amplitudes α, and frequencies ω given in Table 4. Note that the width of the tank limits the experiments to identifying added mass in $y-$direction only. However, as already metnioned, for long slender bodies, the added mass coefficient in $x-$direction is commonly assumed to be zero [8]. The experimental cases are presented in Table 4. The added mass forces can be calculated using (17), where the buoyancy force in $y-$direction as a function of the angle ϕ is given by

$$f_B = B\sin(\phi), \tag{20}$$

where the buoyancy force can be obtained by biasing the sensor data at $\phi = 0$ degrees, where the buoyancy component of the measured force in $y-$direction, f_{m_y}, is zero. During the experiments, for four different values of ϕ, f_{m_y} are measured and the buoyancy force B can be obtained using the following expression:

$$B = \frac{f_{m_y}}{\sin(\phi)}. \tag{21}$$

Removing all of the above terms from (17) the forces caused by the added mass can be obtained. For more details regarding the development experiemntal setups used in this paper, see [11].

Remark 2. *Note that due to the size of the pool and the circulation tank, the experiments are limited to the H1LT and H2LT underwater snake robot configurations in this paper.*

	α [deg]	ω [deg/s]	Fluid flow [m/s]	No. of runs
Case 1	10	60, 70, 80	0.2	3
Case 2	15	60, 70, 80	0.2	3
Case 3	20	60, 70, 80	0.2	3
Simulation scenarios per configuration: 9				
Total number of experimental runs: 18				

TABLE 4: Scenarios for obtaining added mass coefficient in the circulation tank experiments for configurations H1LT and H2LT.

RESULTS

This section presents and discusses the results for the fluid coefficients based on performed simulations and experiments. The results regarding the drag coefficients are obtained from flow simulations in Solidworks, a passive towing tank experimental approach, and circulation tank experiments. The results related to the added mass coefficients are obtained from simulations in WADAM and circulation tank experiments.

Simulation results

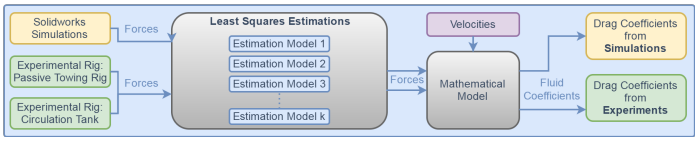

FIGURE 3: Illustration of the work flow for the estimation of the drag coefficients.

The work flow for obtaining the drag coefficients from the forces is illustrated in Figure 3. Solidworks returns forces in body x and y directions for each case of combined input velocity and angle of attack. For each of the nine body configurations, five simulation scenarios are performed (Table 2). The force data generated from the simulations is utilized in a least squares estimation scheme to determine the drag related fluid coefficients. The estimation scheme is applied to both the original model for the drag forces given by (9), and for the various adaptions made to this model given by (10)-(14). Based on all simulation data, each estimation model returns the corresponding fluid coefficients. The obtained simulation results show that the original model $\hat{\mathbf{f}}_1$ together with $\hat{\mathbf{f}}_2$ and $\hat{\mathbf{f}}_6$ are the least successful estimates, but have less error as the snake configuration is extended. The remaining models, $\hat{\mathbf{f}}_3$, $\hat{\mathbf{f}}_4$ and $\hat{\mathbf{f}}_5$ are far more fitting and returns almost the exact same forces. The latter three estimation models all include drag coefficients for the head and tail modules. As the geometry of the head and tail modules are vastly different to the link modules, it is expected that these models tend to be more precise. For larger snake module configurations, the various model variations are quite similar in behaviour [11]. The resulting fluid coefficients obtained for the different estimated force models based on the simulation data are given in Table 5. The resulting coefficients indicate that the force model $\hat{\mathbf{f}}_4$ have the highest correlation in $x-$ and in $y-$direction.

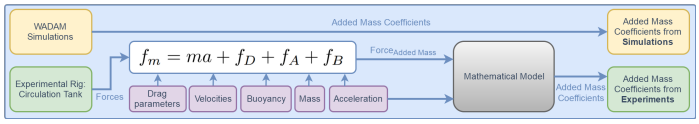

FIGURE 4: Illustration of the work flow for estimation of added mass coefficients.

		$\hat{\mathbf{f}}_1$	$\hat{\mathbf{f}}_2$	$\hat{\mathbf{f}}_3$	$\hat{\mathbf{f}}_4$	$\hat{\mathbf{f}}_5$	$\hat{\mathbf{f}}_6$
Fluid Coefficients	C_f	0.0046					0.2361
	C_d	0.1206					0.4807
	C_f^I		0	0	0	0.0003	
	C_d^I		0.0374	0.0191	0.0191	0.0374	
	C_f^{II}		0.0112	0.0066	0.0066	0.0062	
	C_d^{II}		0.4063	0.4064	0.4064	0.3484	
	$C_{f_{HT}}^I$			0	0.0063		
	$C_{d_{HT}}^I$			0.1956	0.1956		
	$C_{f_{HT}}^{II}$			0.1106	0.1050	0.1134	
	$C_{d_{HT}}^{II}$			0	0	0.6186	
	C_{XY}^I				0.0055		
	C_{XY}^{II}				0.1957	0.1779	

TABLE 5: Fluid coefficients identified based on simulations.

Regarding the added mass coefficients, Figure 4 shows the procedures for the simulation and the experimental approach adopted in this paper. The simulations return the added mass for each of the USR configurations. The $\mu_{x,i}$ and $\mu_{y,i}$ represent the dimensionless added mass parameters in $x-$ and $y-$direction for configuration i, respectively, while the dimensionless $C_{A_{y,i}}$ and $C_{A_{x,i}}$ are commonly referred to as the added mass coefficients, and are dependent on the geometry of the object. The relationship is given by:

$$\begin{aligned} \mu_{x,i} &= V_i \rho C_{A_{x,i}}, \\ \mu_{y,i} &= V_i \rho C_{A_{y,i}}. \end{aligned} \tag{22}$$

The simulation results obtained based on WADAM are summarized in Table 6 together with the volume of each configuration.

Table 6 shows that $\mu_{y,i}$ grows linearly for each added link, while $\mu_{x,i}$ barely increases compared to $\mu_{y,i}$, and is negligible for larger configurations of HnLT. The difference between both dimensionless added mass coefficients, $C_{A_{x,i}}$ and $C_{A_{y,i}}$, are roughly constant for configurations with $n \geq 3$. The simulation results for configurations of the robot with many link modules agrees with the assumption $C_{A_x} = 0$ commonly adopted for slender bodies [8].

Configuration	**Non-dimensionless**		**Dimensionless**		**Volume**
i	$\mu_{x,i}$	$\mu_{y,i}$	$C_{A_{x,i}}$	$C_{A_{y,i}}$	$V_i\,[m^3] \times 10^{-3}$
Head	0.2943	0.2366	0.7631	0.6134	0.376
Link	0.5421	1.2050	0.4170	0.9269	1.268
Tail	0.2683	0.1567	1.0456	0.6108	0.250
HT	0.1837	0.4911	0.2850	0.7620	0.629
H1LT	0.2318	1.8600	0.1195	0.9588	1.893
H2LT	0.5153	3.6840	0.1880	1.3500	2.670
H3LT	0.6486	5.1539	0.1653	1.3132	3.830
H4LT	0.6967	6.7942	0.1379	1.3448	4.929
H5LT	0.9147	8.3451	0.1480	1.3504	6.029
H6LT	0.8570	9.9436	0.1173	1.3606	7.130
H7LT	0.9210	11.527	0.1092	1.3664	8.230
H8LT	1.0449	13.112	0.1093	1.3711	9.330
H9LT	1.1822	14.689	0.1106	1.3740	10.430

TABLE 6: Simulation results for added mass on the different snake modules and configurations.

To obtain an estimated coefficient valid for every snake module configuration, a least square estimation is used on:

$$\begin{aligned} \mu_{x,i} &= V_i \rho \hat{C}_{A_x}, \\ \mu_{y,i} &= V_i \rho \hat{C}_{A_y}, \end{aligned} \tag{23}$$

where $\hat{C}_{A_x}$ and $\hat{C}_{A_y}$ are the unknown coefficients. Similarly, an estimate of the coefficient is obtained using the following expression:

$$\mu_{y,i} = \mu_n \rho n \hat{C}_A, \tag{24}$$

where the coefficient in $x-$direction is neglected. The resulting least square estimations are shown in Table 7. The coefficient $\hat{C}_A$ is smaller than $\hat{C}_{A_y}$. However, the difference is quite small, < 0.1, and smaller than the coefficient in $x-$direction.

$\hat{\mathbf{C}}_{\mathbf{A_x}}$	$\hat{\mathbf{C}}_{\mathbf{A_y}}$	$\hat{\mathbf{C}}_{\mathbf{A_y}}$
0.1194	1.3601	1.2674

TABLE 7: Added mass coefficients from simulation.

Experimental results

The towing rig experiment results in data from the 6-axis force/torque sensor as well as velocities. From the six available measurements, only forces in x and y directions are considered as these are the ones of importance since in this paper we consider a 2D model for USRs. In addition, similarly to the procedure in the previous section concerning the simulation results, system identifications were performed for several model variations. From these experiments, it is observed that most of the estimation models have similar qualitative behaviour as the measured forces. Estimates $\hat{\mathbf{f}}_1$ and $\hat{\mathbf{f}}_2$ seem to be the least fitting in $x-$ and $y-$direction, but behave in the same way for the different weights. Overall, the estimates for model variation $\hat{\mathbf{f}}_4$ seems to be the most fitting model. The resulting fluid coefficients obtained for the different estimated force models based on the passive towing rig data are shown in Table 8.

		$\hat{\mathbf{f}}_1$	$\hat{\mathbf{f}}_2$	$\hat{\mathbf{f}}_3$	$\hat{\mathbf{f}}_4$	$\hat{\mathbf{f}}_5$	$\hat{\mathbf{f}}_6$
Fluid Coefficients	C_f	0.0242					0.4319
	C_d	0.2813					1.7712
	C_f^I		0.0042	0.0109	0.0152	0.0177	
	C_d^I		0.0193	0	0	0.0184	
	C_f^{II}		0.0693	0.0149	0.0045	0	
	C_d^{II}		2.2438	1.5249	1.5249	1.3918	
	$C_{f_{HT}}^I$			0	0		
	$C_{d_{HT}}^I$			0.0795	0.0795		
	$C_{f_{HT}}^{II}$			0.2363	0.2498	0.2556	
	$C_{d_{HT}}^{II}$			1.8852	1.8852	2.4598	
	C_{XY}^I				0.0870		
	C_{XY}^{II}				0.8704	0.3472	

TABLE 8: Fluid coefficients identified based on the passive towing rig experiments.

Compared to the passive towing rig experimental approach, the circulation tank experiments return a large set of measurement data. The reason for this is the extended range of possible fluid flow velocities in the circulation tank. The system identification schemes for the circulation tank experiments are performed with two different data sets as input. The first case includes the entire data set from the experiments, which is in accordance with the system identification schemes for the simulations and the passive towing rig experiment. The second estimation scheme limits the input for the angled experiments to a restricted data set including the results for $\theta \leq 39$ degrees. This is done in order to mitigate the unwanted wall effects obtained from the circulation tank experiments for large θ. Note that $\theta \leq 40$ degrees is a common maximum amplitude for USRs motion patterns [8]. In order to obtain accurate estimates for the added mass coefficient in $y-$direction, accurate drag coefficients are needed. By limiting the data set to $\theta \leq 39$ degrees, the unexpected behaviour in y forces is eliminated and the estimated models should return more accurate results. It is observed that the estimated force models fit satisfactory with the measured forces, however, the restricted data set causes a small improvement in the estimations [11]. The drag coefficients obtained from the circulation tank experiments are shown in Table 9.

Comparison of simulation and experimental results

In general, for both the simulations and experiments, $\hat{\mathbf{f}}_4$ is the most fitting candidate, which is reasonable considering that this

model is the most complex, involving the largest set of individual drag coefficients. Whereas the original model, $\hat{\mathbf{f}}_1$ does in general not produce satisfying results, since this is the simplest model with only two drag coefficients. As $\hat{\mathbf{f}}_2$ includes individual drag coefficients for linear and quadratic drag, it is generally more accurate compared to $\hat{\mathbf{f}}_1$. It is observed that all estimation models struggle to handle the drop in x forces at a large θ. A possible solution is to have drag force equations of a higher polynomial degree. However, as the drag force in x direction for a slender body is small compared to that in y direction, a more complex system may not be necessary, and thus higher accuracy of the model may not be significantly more beneficial. Additionally, from a practical point of view, most common motion patterns for USRs do not involve a value of θ larger than 40-50 degrees, suggesting that the accuracy for large θ to be of low importance.

An interesting observation is that the accuracy of $\hat{\mathbf{f}}_1$ and $\hat{\mathbf{f}}_2$ increases for larger snake module configurations, which implicates that for USRs with many links the original drag force model $\hat{\mathbf{f}}_1$ may be of similar accuracy as the more complex models such as $\hat{\mathbf{f}}_4$. In addition, it is observed that the effects of the drag forces caused by the head and tail gradually decreases with an increasing number of links. Considering the results for $\hat{\mathbf{f}}_4$ in Table 10, it is clear that the coefficients for quadratic drag dominate the coefficients for linear drag. This might indicate that $\hat{\mathbf{f}}_4$ could be simplified by removing some of the linear terms. The resulting drag coefficients for $\hat{\mathbf{f}}_1$ are presented in Table 11. Comparing these results to the analytical estimates in Remark 1, the experimental results for C_f are closer to the analytical estimates than what was identified based on the simulations. On the other hand, the values for C_d are much smaller for both experiments and simulations compared to Remark 1.

		$\hat{\mathbf{f}}_1$	$\hat{\mathbf{f}}_2$	$\hat{\mathbf{f}}_3$	$\hat{\mathbf{f}}_4$	$\hat{\mathbf{f}}_5$	$\hat{\mathbf{f}}_6$
	C_f	0.0207					0.3363
	C_d	0.3268					1.6066
	C_f^I		0	0	0	0.0032	
	C_d^I		0.0603	0	0	0.0602	
	C_f^{II}		0.0544	0.0133	0.0133	0.0088	
	C_d^{II}		1.8601	1.4272	1.4272	1.1142	
Fluid Coefficients	$C_{f_{HT}}^I$			0	0.0148		
	$C_{d_{HT}}^I$			0.1769	0.1769		
	$C_{f_{HT}}^{II}$			0.2602	0.2451	0.2675	
	$C_{d_{HT}}^{II}$			1.1770	1.1770	2.0963	
	C_{XY}^I				0.0351		
	C_{XY}^{II}				0.4612	0.2963	

TABLE 9: Fluid coefficients identified based on the circulation tank experiments based on restricted dataset.

Remark 3. *From the obtained results we see that for small snake module configurations, the effects from the head and tail modules, as well as the x-y cross forces have a significant presence compared to the effects caused by the link modules alone. Hence, it is necessary for a complex drag force model with several drag-related individual drag coefficients to be incorporated to sufficiently describe the resulting fluid forces. However, for larger snake module configurations, a more simple model is sufficient such as the one proposed in [8] as it was indicated from the simulation studies and experiments with larger configurations.*

		Passive	**Circulation Tank**	
	Simulated	**Towing Rig**	Unrestricted	Restricted
C_f^I	0	0.0152	0	0
C_f^{II}	0.0191	0	0.0569	0
C_d^I	0.0066	0.0045	0.0126	0.0133
C_d^{II}	0.4064	1.5249	1.2402	1.4272
$C_{f_{HT}}^I$	0.0063	0	0.0141	0.0148
$C_{d_{HT}}^I$	0.1956	0.0795	0.1929	0.1769
$C_{f_{HT}}^{II}$	0.1050	0.2498	0.2531	0.2451
$C_{d_{HT}}^{II}$	0	1.8852	1.4444	1.1770
C_{XY}^I	0.0055	0.0870	0.0412	0.0351
C_{XY}^{II}	0.1957	0.8704	0.6654	0.4612

TABLE 10: Comparison of drag coefficients for force model, $\hat{\mathbf{f}}_4$.

		Passive	**Circulation Tank**	
	Simulated	**Towing Rig**	Unrestricted	Restricted
C_f	0.0046	0.0242	0.0167	0.0207
C_d	0.1206	0.2813	0.3835	0.3628

TABLE 11: Comparison of drag coefficients for force model, $\hat{\mathbf{f}}_1$.

The added mass coefficients identified based on the performed simulations and experiments are shown in Table 12. From the simulation, the added mass coefficient in $x-$direction has an expected low value and a theoretical value of the added mass parameter $\mu_t = 0$ is reasonable for modelling purposes, especially for large snake module configurations. Comparing the simulation and experimental results, the resulting added mass coefficients are of similar values. This indicates that the simulation results can be used to properly identify the added mass coefficients. Note that the obtained fluid parameters in Table 12 are within the range of the analytical estimates in Remark 1.

	Simulations	**Circulation Tank**
C_{A_x}	0.1194	-
C_{A_y}	1.3601	-
C_A	1.2674	1.2770

TABLE 12: Comparison of added mass coefficients.

The results obtained for the added mass coefficients from the experiment rely on the experimentally obtained fluid drag coefficients. For the estimation, two different drag models estimates based on the drag experiments are used. This is done

as a means to investigate how different drag force estimates influence the added mass estimations. The drag force models in question are $\hat{\mathbf{f}}_1$ and $\hat{\mathbf{f}}_4$. The least square estimation uses the expression given by (24). The result of the estimations is presented in Table 13, where it is clear that the resulting coefficients varies insignificantly based on which drag force model is used. The obtained values are close to the theoretical value $C_A \in [1, 1.5]$ as mentioned in Remark 1.

Drag model	C_A
$\hat{\mathbf{f}}_1$	1.2754
$\hat{\mathbf{f}}_4$	1.2770

TABLE 13: Added mass coefficients from circulation tank experiments, based on different drag force models.

CONCLUSIONS

This paper presents general methods for identifying fluid coefficients for USRs based on both CFD simulations and several experimental approaches. The fluid force model presented in [8] is used to identify the parameters for the hydrodynamic model. Additionally, different variations and extensions to the hydrodynamics model proposed in [8] are presented. It is observed that the original drag force model in [8] correlates to the results obtained in this paper for large snake module configurations, indicating that the closed-form analytical model of USRs presented in [8] is suitable for snake module configurations with many links. Based on the different experimental results, the drag force coefficients for the model presented in [8] are identified as $C_f \in [0.02, 0.03]$ which is in accordance with the theoretical estimates, and $C_d \in [0.2, 0.4]$ which is smaller than the expected theoretical values. This paper shows that the added mass coefficient for the underwater snake robot Mamba is $C_A \approx 1.27$, which is in agreement with the existing analytical estimates for USRs. In the future, the experiments and simulation schemes presented in this paper will be extended for fluid coefficients identification for a 3D model of USRs.

References

[1] Fossen, T. I., 2011. *Handbook of Marine Craft Hydrodynamics and Motion Control*. Wiley, New York.

[2] Kelasidi, E., Liljebäck, P., Pettersen, K. Y., and Gravdahl, J. T., 2016. "Innovation in underwater robots: Biologically inspired swimming snake robots". *IEEE Robotics and Automation Magazin,* ***23***(1), pp. 44–62.

[3] Hirose, S., 1993. *Biologically Inspired Robots: Snake-Like Locomotors and Manipulators*. Oxford University Press.

[4] Liljebäck, P., Pettersen, K. Y., Stavdahl, Ø., and Gravdahl, J. T., 2013. *Snake Robots: Modelling, Mechatronics, and Control*. Springer-Verlag, Advances in Industrial Control.

[5] Kelasidi, E., Liljebäck, P., Pettersen, K. Y., and Gravdahl, J. T., 2015. "Experimental investigation of efficient locomotion of underwater snake robots for lateral undulation and eel-like motion patterns". *Robotics and Biomimetics,* ***2***(1), pp. 1–27.

[6] Kelasidi, E., Pettersen, K. Y., and Gravdahl, J. T., 2015. "Energy efficiency of underwater robots". In Proc. 10th IFAC Conference on Manoeuvring and Control of Marine Craft (MCMC), pp. 152–159.

[7] Kelasidi, E., Pettersen, K. Y., Gravdahl, J. T., and Liljebäck, P., 2014. "Modeling of underwater snake robots". In Proc. IEEE International Conference on Robotics and Automation (ICRA), pp. 4540–4547.

[8] Kelasidi, E., Pettersen, K. Y., Gravdahl, J. T., Strømsøyen, S., and Sørensen, A., 2017. "Modeling and propulsion methods of underwater snake robots". In Proc. 1st IEEE Conference on Control Technology and Applications, pp. 819–826.

[9] Khalil, W., Gallot, G., and Boyer, F., 2007. "Dynamic modeling and simulation of a 3-d serial eel-like robot". *Systems, Man, and Cybernetics, Part C: Applications and Reviews, IEEE Transactions on,* ***37***(6), pp. 1259–1268.

[10] Doraiswami, R., Diduch, C., and Stevenson, M., 2014. *Linear Least Squares Estimation*. Chichester, UK: John Wiley & Sons, Ltd, Chichester, UK.

[11] Elgenes, G., and Kilvær, H., 2017. "Underwater robotics - fluid parameter identification for modelling of underwater snake robots". Master's thesis, NTNU, https://brage.bibsys.no/xmlui/handle/11250/2451323.

[12] Lopez-Pavon, C., and Souto-Iglesias, A., 2015. "Hydrodynamic coefficients and pressure loads on heave plates for semi-submersible floating offshore wind turbines: A comparative analysis using large scale models". *Renewable Energy,* ***81***, pp. 864–881.

[13] Liagre, P. F., and Niedzwecki, J. M., 2003. "Estimating nonlinear coupled frequency-dependent parameters in offshore engineering". *Applied Ocean Research,* ***25***(1), pp. 1–19.

[14] Eng, Y., Lau, W., Low, E., Seet, G., and Chin, C., 2008. "Estimation of the hydrodynamics coefficients of an rov using free decay pendulum motion". *Engineering Letters,* ***16***(3), pp. 326–331.

[15] Huse, E., 1994. *Experimental methods in marine hydrodynamics*. NTNU.

[16] Lee, S., Park, J., and Han, C., 2007. "Optimal control of a mackerel-mimicking robot for energy efficient trajectory tracking". *Journal of Bionic Engineering,* ***4***(4), pp. 209–215.

[17] Eidsvik, O. A., and Schjlberg, I., 2015. "Identification of hydrodynamic parameters for remotely operated vehicles". Master's thesis, NTNU.

[18] Millan, David; Thornburn, P., 2010. "A planar motion mechanism (pmm) for ocean engineering studies". In 18th Newfoundland Electrical and Computer Engineering Conference, Canada.